Broadband, angle-dependent optical characterization of asymmetric self-assembled nanohole arrays in silver

Z. El-Ansary (✉ zakaria.elansary@uit.ac.ma)

Ibn-Tofaïl University

H. P. R. Kumar

Sapienza Università di Roma

B. Brioual

ERCMN, FSTT, Abdelmalek Essâadi University

E. Petronijevic

Sapienza Università di Roma

T. Cesca

University of Padova

C. Scian

University of Padova

G. Mattei

University of Padova

M. El Hasnaoui

Ibn-Tofaïl University

C. Sibilia

Sapienza Università di Roma

A. Belardini

Sapienza Università di Roma

Research Article

Additional Declarations: No competing interests reported.

Abstract

Plasmonic nanostructured materials made of nanohole arrays in metal are significant plasmonic devices exhibiting resonances and strong electromagnetic confinement in the visible and near-infrared range. As such, they have been proposed for use in many applications such as biosensing and communications. In this work, we introduce the asymmetry in nanoholes, and investigate its influence on the electromagnetic response by means of broadband experimental characterization and numerical simulations. As a low-cost fabrication process, we use nanosphere lithography, combined with tilted silver evaporation, to obtain a 2D hexagonal array of asymmetric nanoholes in Ag. Our experimental set-up is based on a laser, widely tunable in the near-infrared range, with precise polarization control in the input and in the output. We next resolve the circular polarization degree of the transmitted light when the nanohole array is excited with linear polarization. We attribute the disbalance of left and right transmitted light to the asymmetry of the nanohole, which we support by numerical simulations. We believe that the optimization of such simple plasmonic geometry could lead to multifunctional flat-optic devices.

1 Introduction

Over the past three decades, researchers have become increasingly interested in the physics of light-matter interaction metal films, corrugated in a periodic manner. Periodic arrays of nanovoids, such as nanohole arrays (NHA), can couple light to surface plasmon polaritons (SPPs) (Barnes et al. 2003) and exhibit extraordinary optical transmission (EOT) (Ebbesen at al. 1998; García de Abajo 2007), at the same time leading to electromagnetic confinement at the nanoscale. The electromagnetic field is enhanced at the metal-dielectric contact as a result of these particular resonant electromagnetic excitations, which are tightly spatially restricted. The periodicity of the array, the materials surrounding the patterned metal, and the materials used to create it all have a significant impact on the resonant optical response of the system. This enabled many demonstrations and application proposals in subwavelength optics (Barnes et al. 2003; Ni et al. 2013), surface enhanced Raman spectroscopy (Luo et al. 2019), and emission rate modification (Michieli et al. 2018), chemical and biosensing (Escobedo 2013; Couture at al. 2019; Vala et al. 2019)

Additional degree of freedom is enabled when the symmetry of the NHA-light interaction is broken, which opens the possibility to obtain optical chirality at the nanoscale (Valev et al. 2013; Hentschel et al. 2017; Schäferling et al. 2012). NHA can differently interacts with circular polarizations of opposite handedness, leading to important consequences at both near- and far-field spatial scales. Anisotropy in the planar nanohole shape naturally gives rise to polarization-dependent EOT (Di Maio et al.2006; Ai et al. 2017) as well as in the near-field chirality (Triolo et al. 2019), while 3D anisotropy leads to true, giant chiral signals (Kondratov et al. 2016; Ai et al. 2020). A simple approach to obtain an in-plane asymmetry which still leads to chiral properties is to tilt the elliptical nanohole from the symmetry lines of the array; such elliptical nanohole arrays (ENHA) were first numerically predicted to give differential absorption for left and right circularly polarized excitation (LCP and RCP, respectively), i.e. circular dichroism (CD) (Petronijevic et al. 2019). Petronijevic and co-authors then experimentally showed that an ENHA in metal

can lead to a low extinction CD at normal incidence (Petronijevic et al. 2020a). And further numerically optimized it in the near-infrared range (Petronijevic et. 2020b).

Inspired by the previously shown chiral properties in the ENHA extinction, in this work we investigate polarization properties of the light transmitted through asymmetric ENHA; we excite the sample with linear polarization and investigate the transmitted polarization. We use the ENHA patterned in Ag, obtained by means of inexpensive nanosphere lithography (NSL), combined with asymmetric Ag deposition. We measure optical properties across the near-infrared range by exciting the sample with a widely tunable laser (700–1000 nm range). Even though the inherent chirality of our ENHA is minimal, the intrinsic asymmetry still leads to the disbalance between LCP and RCP in the transmitted signal, in a wide range of incidence angles and excitation wavelengths. We further employ numerical simulations to gain more insight into the origin of chiro-optical disbalance of the transmitted signal. We finally propose how such simple and low-cost geometry can be optimized at a given wavelength to work as a circularly polarizing device.

2 Materials And Methods

2.1 Fabrication

Plasmonic NHA and other plasmonic shapes can be made by means of self-assembling, low-cost and time-efficient NSL (Michieli et al. 2018; Petronijevic et al. 2020a; Murray-Methot et al. 2008; Belardini et al. 2014; Cheng et al. 2012; Zhang et al. 2022; Petronijevic et al. 2021a; Leahu et al. 2021), providing large-area plasmonic samples with hexagonal unit cell. In this study, we use a self-assembled 2D meta surface of polystyrene nanospheres (PSN) with starting diameter of 518 nm; the initial diameter determined the final plasmonic structure's lattice periodicity. After that, the initial PNS diameter was decreased to 356 nm using reactive ion etching (RIE), while keeping the ordered arrangement. The short axis length of the final nano ellipse is determined by this reduced diameter D_s. Then, a layer of 55 nm Ag was deposited by 45° angled magnetron sputtering, introducing an additional in-plane tilt (Petronijevic et al. 2020a). The angled Ag sputtering results in the asymmetric shadow on the substrate, which elongates one of the nanohole's diameters (D_l). In order to obtain ENHA, as the final step we removed PSNs by dissolving them in toluene; the Scanning Electron Microscopy (SEM) image of the resulting sample is shown in the inset of Fig. 1.

2.2 Measurements

In the previous work (Petronijevic et al. 2020a) it was shown how the symmetry breaking in these arrays happens because of combining effects: elliptical shape of the nanohole, and a slight in-plane of the ellipse axis with respect to the lines of hexagonal symmetry. These effects led to a rather low extinction CD in the near-infrared range, as the ENHA shape parameters were not optimized. Here, we investigate how the asymmetric shape of the nanohole influences the output beam polarization. Figure 1 shows the experimental set-up with the following components: a broadly adjustable near-infrared laser (Chameleon Ultra II from Coherent Inc, Santa Clara, CA, USA), a linear polarizer (LP), a rotation stage with the sample,

a quarter wave plate (QWP) and another LP for the output beam, and, finally, a Si photodiode (PD). We measure wavelengths ranging from 700 nm to 1000 nm. The pulse length of this laser is 140 fs, with a repetition rate of 80 MHz. We employed a mechanical chopper at 70 Hz to obtain the linear characterization mode. A beam-splitter (using 4% of the output laser power) and appropriate natural density filters reduced the power before impinging on the sample. The LP and QWP components were optimally chosen for the investigated near-infrared range. The linearly polarized field (p-polarization) impinges on the sample at various angles of incidence θ, by rotating the sample between – 45° and 45°. The polarization of the transmitted light is then resolved by rotating QWP (from – 90° to 90°) and passing such beam through the second LP. The measurements are done at room temperature.

3 Results

3.1 Experiments

In Fig. 2a, we show the wavelength-incidence angle map when the sample is excited with linearly p-polarized light, and the QWP angle in the output is set to zero (linearly polarized output). We notice transmission minima features, strongly dependent on the incidence angle, which correspond to coupling of the light to surface plasmon polaritons (Petronijevic et al. 2017). When the sample is fixed at the angle of θ = 0°, the transmission intensity is moderately high for longer wavelengths, with specific transmission dip around 700 nm. Then, as the sample angle is gradually altered, the transmission decreases significantly. Note that here only the zeroth order of transmission is resolved, while other techniques such as photo-deflection can be used to monitor the diffraction effects in such asymmetric samples (Leahu et al. 2021). At 800 nm, we choose three angles of incidence (indicated by stars), and further study how the transmitted intensity changes with QWP rotation.

Hence, we fix the excitation wavelength at 800 nm, and we rotate the QWP, at three chosen points of incidence. Figure 2b shows the transmission intensity dependance on the QWP rotation at -25°, 0° and 25° angles of incidence, where all the results are normalized to the respective maximum value; -45° and 45° of the QWP angle correspond to LCP and RCP, respectively. We note that light is transmitted to LCP more than to RCP, with the difference of around 0.15. This means that the sample introduces a disbalance in the outgoing optical field polarization, which does not exit the sample with the linear polarization, even though it is excited with p-polarized light. Moreover, LCP to RCP difference does not invert with the inversion of the incidence angle, which would be a feature of extrinsic chirality (Leahu et al. 2017). Next, we perform the complete spectral characterization at constant QWP angles corresponding to LCP and RCP. Figure 2c-d shows that over a broadband range, and at various incidence angles, light gets transmitted to LCP more than to RCP. All the transmission maps are normalized to the signal obtained with QWP at 0° without the sample.

Next, we plot the difference of the signal transmitted to the LCP and RCP, defining it as $\Delta T = T_{toLCP} - T_{toRCP}$; the results are shown in Fig. 3a. In the shortest wavelength range (700−720 nm), around normal incidence, the light gets transmitted into linear polarization, as the difference

between LCP and RCP drops to zero; going to the oblique incidence, ΔT increases. On the other side, at all near-infrared ranges, transmission to LCP prevails, and the difference decreases for oblique incidence. There are no specific resonant features in ΔT; interestingly, this sample showed only a low extinction CD, which was attributed to the unoptimized geometric parameters in ref. (Petronijevic et al. 2020a). In Fig. 3b, we display spectra at oblique incidence θ = 25° for a full rotation of QWP of -90° to 90°; results are normalized to the spectrum of the sample at θ = 25° with QWP at 0°. A stronger transmission at RCP with respect to LCP appears throughout the whole spectrum.

3.2 Simulations

To gain more insight into the origin of the measured asymmetry, we further perform numerical simulations using the 3D Finite Difference Time Domain (FDTD) method by Lumerical commercial software (Lumerical Solutions, Inc). The chiro-optical properties of elliptic Ag-NHAs were numerically investigated by defining a rectangular unit cell (a and $a\sqrt{3}$, where $a = 518nm$), representative of the hexagonal nanoholes base cell, with Bloch boundary conditions in the xy-plane, and perfectly matched layer boundary conditions in the z-direction. In the upper part of Fig. 4a we show the xy cross-section of the simulated cell. A semi-infinite rectangle is first defined to simulate the glass substrate with a refractive index of 1,5 covered with 55 nm thick silver film (the complex refractive index of Silver is taken from the ellipsometry measurements in ref. (Petronijevic et al. 2020b). The nanoellipse hole in the metal layer is defined with long and short diameters D_l and D_s, and with the tilt φ of the long diameter with respect the hexagonal symmetry axis; this shape "etches" the Ag layer at positions forming hexagonal symmetry. In the bottom part of Fig. 4a, we show 3D sketch of the simulation set-up which mimics the experimental set-up. We excite the sample from the air with a linearly (p) polarized source; note that we set this polarization to be always in the x-direction of the simulation set-up, while we can change the nanoellipse tilt angle φ. Therefore, the linearly polarized light excites the ENHA, and the transmitted field impinges on the polarization ellipse analysis group, which resolves the polarization and ellipticity of the outcoming beam (the script can be found in "polarztn_ellipse" details of the solver). As in the experiment, we focus only on the zeroth order. The result of this analysis is the plot of the polarization ellipse, which is defined by the major and minor axes, angle ψ (which describes the tilt of the major axis with respect to the p-polarized direction), and handedness. Another feature investigated by this simulation set-up is the absorption CD; in this case, to simulate circular polarization, two linear x- and y-polarized plane-wave sources were made with a phase difference of 90° and − 90° corresponding to RCP and LCP polarizations, respectively. The total absorption by the silver ENHA is calculated by integrating the absorption density ρ_{abs} over the unit cell volume.

We start by simulating the ENHA with $D_s = 356nm$, and $D_l = 380nm$, as such low difference in the ellipse axes corresponds to the real sample investigated here. In Fig. 4b we show the output polarization ellipse, i.e. the ellipse described by the electric field vector in time, when the ENHA is excited at 800 nm, and φ is varied. For $\varphi = 0°$, only linear dichroism exists in such sample; therefore, the x-polarized incident light keeps this polarization when transmitted to the glass. However, a tilting of the sample to $\varphi = 10°$, and $\varphi = 20°$ introduces an increasing ellipticity. Next, we set $\varphi = 28°$ (Petronijevic et al.

2020a), and we investigate the influence of the changing D_l starting from a circular NHA ($D_s = D_l = 356nm$). As expected, the circular shape does not change the polarization, while $D_l = 404nm$ introduces a considerable ellipticity of the output polarization, Fig. 4c.

We next investigate the wavelength dependence of the ellipse parameters which will lead to the optimization of the sample geometry. At normal incidence, the polarization ratio is defined as the ratio of the power transmitted to the x- and y-directed polarizations, respectively (i.e. the ratio between p- and s-polarizations). High polarization ratios mean that the ENHA does not change the incident polarization, while the polarization ratio approaching 1 means that the ENHA transmits linear to circular polarization. In Fig. 5a, we show the extracted values of the polarization ratio for different ENHA. For the unoptimized ENHA, as in our sample, the parameters are $\varphi = 28°$, $D_l = 380nm$, and $D_s = 356nm$. The minimum polarization ratio (~ 7) lies around 690 nm, just below our measurement range, and strongly increases to 15 around 700 nm. This agrees well with the ΔT drop in the short wavelength range (no considerable difference between LCP and RCP in the output). Next, we perform the first optimization to lower the polarization ratio minimum; we use the ENHA analysis from ref. (Petronijevic et al. 2020b; Petronijevic et al. 2021b), where absorption CD of ENHA was studied in detail. In those works, ENHA showed strong chiral behavior when diameters scaled as $D_l = a$, and $D_s = 280a/500$, while the tilt angle was kept at $\varphi = 15°$, and the metal thickness was 100 nm. Scaled with $a = 518nm$, we calculated the polarization ratio for such strongly elliptical ENHA. The first optimization leads to the polarization drop to 1.5 at 690 nm (blue line in Fig. 5a). Note that this scaling of parameters was first investigated in Au-ENHA in (Petronijevic et al. 2020b), and then applied to Ag-ENHA (Petronijevic et al. 2020b). Therefore, we perform Optimization 2 for Ag to shift the optimal lowest polarization to the range of our measurements. To this end, we optimize absorption CD in terms of D_l, D_s, φ and Ag thickness in the near-infrared range. The resulting parameters are $D_l = 513nm$, $D_s = 280nm$, $\varphi = 15°$, and the Ag thickness of 55 nm. The optimum polarization ratio is as low as 1.1 at 750 nm (red line in Fig. 5(a)). Away from the resonant features (where also absorption CD drops), the polarization ratio increases, meaning that the polarization state of the input beam does not get significantly altered.

In Fig. 5b-d we show the resulting polarization ellipses for the three Ag-ENHA, at the wavelengths of the polarization ratio minima. As expected, the unoptimized sample gives the elliptical polarization mostly in x-direction when excited by x-polarized light at 690 nm, Fig. 5b. On the other hand, Optimization 1 leads to the transmission of x-polarized light to a left elliptical polarization which approaches LCP, Fig. 5c. Finally, Optimization 2 moves the polarization ratio minimum to 750 nm, when the linearly polarized excitation is transmitted to almost perfect LCP. We conclude that the strongly elliptical shape and proper in-plane tilt cause this simple geometry to work as a resonant circular polarizer within tens of nm of metal, Fig. 5d.

4 Conclusion

In this paper, we reported on the asymmetric transmission of low-cost nanohole arrays in silver, by means of experimental and numerical methods. The investigated sample was fabricated by a low-cost, self-assembling NSL, and a tilted angled deposition led to a slightly elliptical and asymmetric shape of the

nanoholes. We then excited the sample with the linearly polarized beam and measured the transmission to the LCP or RCP, by placing the polarizing components in the output before the detector. We performed broadband characterization in the near-infrared region, which showed the difference between LCP and RCP in the output. We then applied numerical approach to understand how the ENHA shape influences this difference. Finally, we showed that this simple geometry can be optimized in the near-infrared range, for linear-to-circular polarization conversion.

Declarations

Acknowledgements

Ethical Approval We agreed all terms and conditions for Ethics approval.

Competing interests The authors declare that have no conflict of interests.

Author contributions

Z.E.: is the author; he made the experimental part and wrote the article with the help of all co-authors.

H.P.R.K.: participated in the experimental part.

B.B.: performed numerical simulations.

E.P.: mentored the experiments, and performed additional simulations.

T.C.: participated in fabrication of the sample

C.S.: participated in fabrication of the sample

G.M.: participated in fabrication of the sample

M.E.: is the supervisor of thesis preparation.

C.S.: is the supervisor of the Erasmus+ exchange on Roman side.

A.B.: organized experimental set-up and supervised the experiments.

All authors reviewed the manuscript.

Availability of data and materials No confidential and non IP Materials and data will be available upon request.

References

1. Ai, B., Basnet, P., Larson, S., Ingram, W., Zhao, Y.: Plasmonic Sensor with High Figure of Merit Based on Differential Polarization Spectra of Elliptical Nanohole Array. Nanoscale. **9**, 14710–14721 (2017)

2. Ai, B., Luong, H.M., Zhao, Y.: Chiral Nanohole Arrays. Nanoscale. **2**, 2479–2491 (2020)

3. Barnes, W.L., Dereux, A., Ebbesen, T.W.: Surface plasmon subwavelength optics. Nature. **424**, 824–830 (2003)

4. Belardini, A., Benedetti, A., Centini, M., Leahu, G., Mura, F., Sennato, S., Sibilia, C., Robbiano, V., Giordano, M.C., Martella, C., Comoretto, D., de Buatier, F.: Second Harmonic Generation Circular Dichroism from Self-Ordered Hybrid Plasmonic–Photonic Nanosurfaces. Adv Opt. Mater. **2**, 208–213 (2014)

5. Couture, M., Ray, K.K., Poirier-Richard, H.P., Crofton, A., Masson, J.: f.: 96-Well Plasmonic Sensing with Nanohole Arrays. ACS Sens. **1**, 287–294 (2016)

6. Cheng, K., Wang, S., Cui, Z., Li, Q., Dai, S., Dua, Z.: Large-scale fabrication of plasmonic gold nanohole arrays for refractive index sensing at visible region. Appl. Phys. Lett. **100**, 253101 (2012)

7. Di Maio, J.R., Ballato, J.: Polarization-dependent transmission through subwavelength anisotropic aperture arrays. Opt. Express. **14**, 2380–2384 (2006)

8. Ebbesen, T.W., Lezec, H.J., Ghaemi, H.F., Thio, T., Wolff, P.A.: Extraordinary optical transmission through sub-wavelength hole arrays. Nature. **391**, 667–669 (1998)

9. Escobedo, C.: On-chip nanohole array based sensing: a review. Lab. Chip. **13**, 2445–2463 (2013)

10. García de Abajo, F.J.: Colloquium: light scattering by particle and hole arrays. Rev. Mod. Phys. **79**, 1267–1290 (2007)

11. Hentschel, M., Schäferling, M., Duan, X., Giessen, H., Liu, N.: Chiral plasmonics.Sci. Adv.3, e1602735 (2017)

12. Kondratov, A.V., Gorkunov, M.V., Darinskii, A.N., Gainutdinov, R.V., Rogov, O.Y., Ezhov, A.A., Artemov, V.V.: Extreme optical chirality of plasmonic nanohole arrays due to chiral Fano resonance. Phys. Rev. B. **93**, 195418 (2016)

13. Leahu, G., Petronijevic, E., Li Voti, R., Belardini, A., Cesca, T., Mattei, G., Sibilia, C.: Diffracted beams from metasurfaces: high chiral detectivity by photothermal deflection technique. Adv. Opt. Mater. **9**, 2100670 (2021)

14. Leahu, G., Petronijevic, E., Belardini, A., Centini, M., Sibilia, C., Hakkarainen, T., Koivusalo, E., Rizzo Piton, M., Suomalainen, S., Guina, M.: Evidence of Optical Circular Dichroism in GaAs-Based Nanowires Partially Covered with Gold. Adv. Opt. Mater. **5**, 1601063 (2017)

15. Lumerical Solutions, Inc:. http://www.lumerical.com/tcad-products/fdtd/

16. Luo, X., Xing, Y., Galvan, D.D., Zheng, E., Wu, P., Cai, C., Yu, Q.: Plasmonic Gold Nanohole Array for Surface-Enhanced Raman Scattering Detection of DNA Methylation. ACS Sens. **4**, 1534–1542 (2019)

17. Michieli, N., Kalinic, B., Scian, C., Cesca, T., Mattei, G.: Emission Rate Modification and Quantum Efficiency Enhancement of Er3 + emitters by Near-Field Coupling with Nanohole Arrays". ACS Photonics. **5**, 2189–2199 (2018)

18. Murray-Methot, M., Menegazzo, N., Masson, J.: Analytical and physical optimization of nanohole-array sensors prepared by modified nanosphere lithography. Analyst. **133**, 1714–1721 (2008)

19. Ni, X., Ishii, S., Kildishev, A.V., Shalaev, V.M.: Ultra-thin, planar, Babinet-inverted plasmonic metalenses.Light Sci Appl.2, e72 (2013)

20. Petronijevic, E., Leahu, G., Li Voti, R., Belardini, A., Scian, C., Michieli, N., Cesca, T., Mattei, G., Sibilia, C.: Photo-acoustic detection of chirality in metal-polystyrene metasurfaces. Appl. Phys. Lett. **114**, 053101 (2019)

21. Petronijevic, E., Belardini, A., Leahu, G., Cesca, T., Scian, C., Mattei, G., Sibilia, C.: Circular dichroism in low-cost plasmonics: 2D arrays of nanoholes in silver. Appl. Sci. **10**, 1316 (2020a)

22. Petronijevic, E., Ali, H., Zaric, N., Belardini, A., Leahu, G., Cesca, T., Mattei, G., Andreani, L.C., Sibilia, C.: Chiral effects in low–cost plasmonic arrays of elliptic nanoholes. Opt. Quant. Electron. **52**, 176 (2020b)

23. Petronijevic, E., Belardini, A., Cesca, T., Scian, C., Mattei, G., Sibilia, C.: Rich near-infrared chiral behavior in diffractive metasurfaces. Phys. Rev. Appl. **16**, 014003 (2021a)

24. Petronijevic, E., Leahu, G., Mussi, V., Sibilia, C., Bovino, A.F.: Photoacoustic technique for the characterization of plasmonic properties of 2D periodic arrays of gold nanoholes. AIP Adv. **7**, 025210 (2017)

25. Petronijevic, E., Ghahri, R., Sibilia, C.: Plasmonic Elliptical Nanohole Arrays for Chiral Absorption and Emission in the Near-Infrared and Visible Range". Appl. Sci. **11**, 6012 (2021b)

26. Schäferling, M., Dregely, D., Hentschel, M., Giessen, H.: Tailoring Enhanced Optical Chirality: Design Principles for Chiral Plasmonic Nanostructures. Phys. Rev. X. **2**, 031010 (2012)

27. Triolo, C., Savasta, S., Settineri, A., Trusso, S., Saija, R., Agarwal, N.R., Patanè, S.: Near-feld imaging of surface-plasmon vortex-modes around a single elliptical nanohole in a gold film. Sci. Rep. **9**, 5320 (2019)

28. Vala, M., Ertsgaard, C.T., Wittenberg, N.J., Oh, S.: Plasmonic Sensing on Symmetric Nanohole Arrays Supporting High–Q Hybrid Modes and Reflection Geometry. ACS Sens. **4**, 3265–3274 (2019)

29. Valev, V.K., Baumberg, J.J., Sibilia, C., Verbiest, T.: Chirality and chiroptical effects in plasmonic nanostructures: Fundamentals, recent progress, and outlook. Adv. Mater. **25**, 2517–2534 (2013)

30. Zhang, Z., Zhao, F., Gao, R., Jao, C., Ma, C., Li, J., Li, X., Guan, B., Cetin, A.E., Chen, K.: Rayleigh anomaly-enabled mode hybridization in gold nanohole arrays by scalable colloidal lithography for highly-sensitive biosensing. Nanophotonics. **11**, 507–517 (2022)
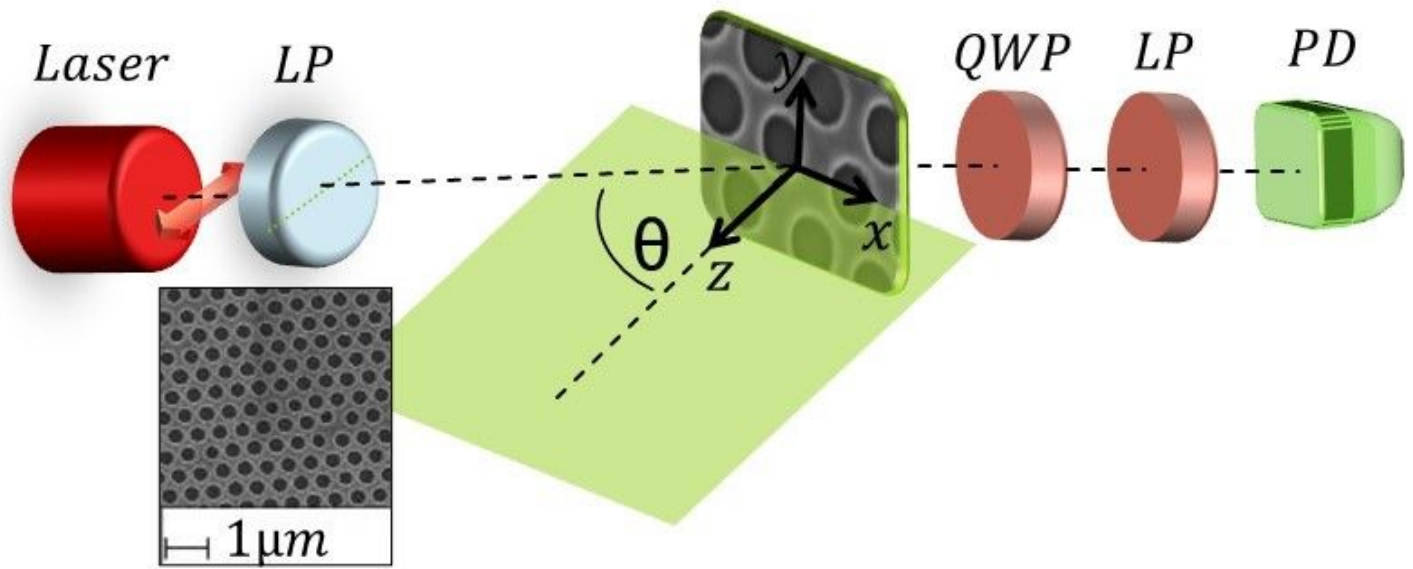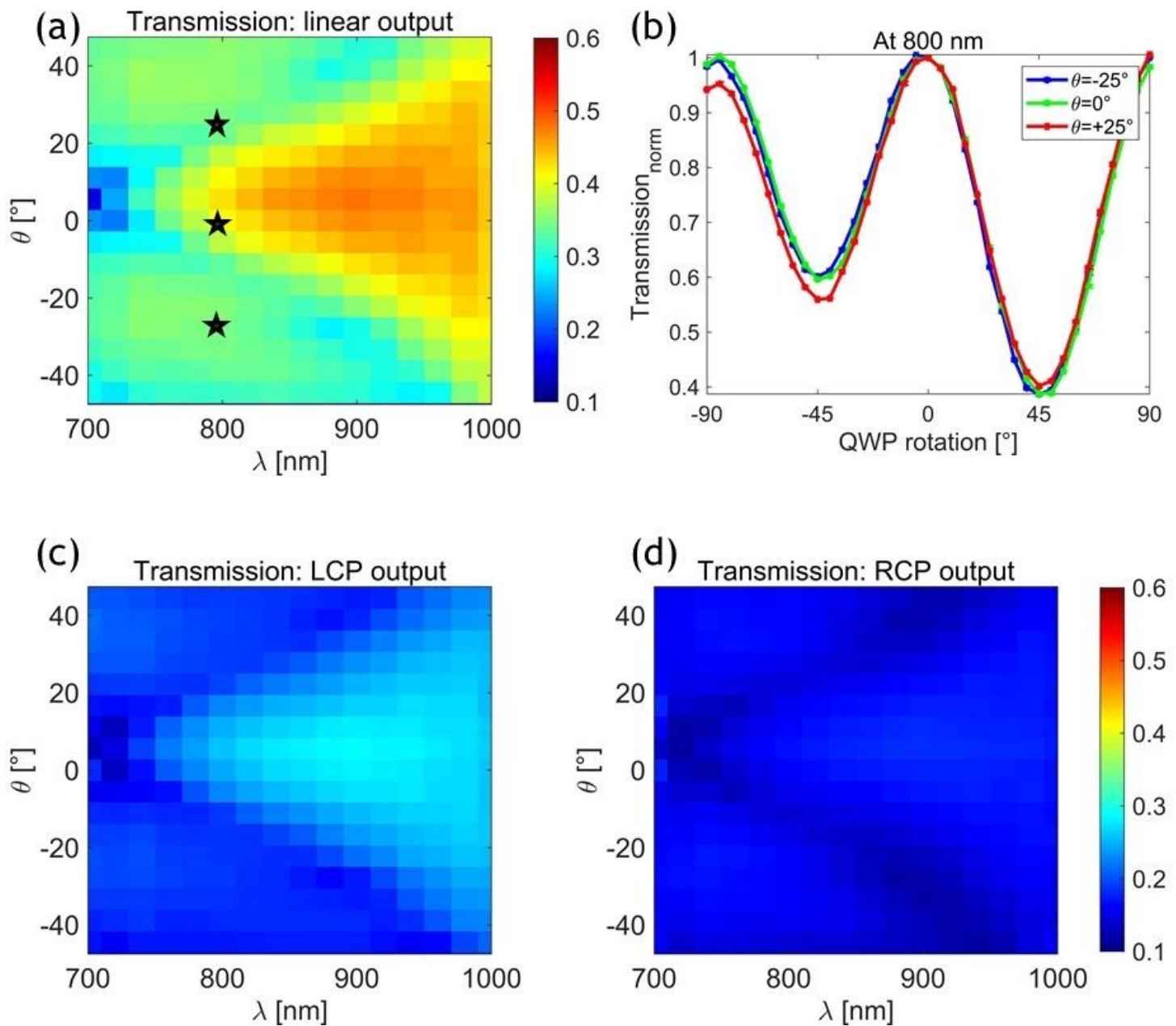
Figures

Figure 1

Sketch of the experimental set-up; inset: SEM image of the sample

Figure 2

a Experimental λ-θ Transmission map for linearly polarized excitation; stars denote chosen incidence angles at 800 nm, for the following investigation of QWP rotation dependence; b The transmission dependence on QWP rotation at λ=800nm, at -25°, 0° and 25° angles of incidence, normalized to their respective maxima; c and d Experimental λ-θ Transmission maps for LCP, and RCP excitations respectively.
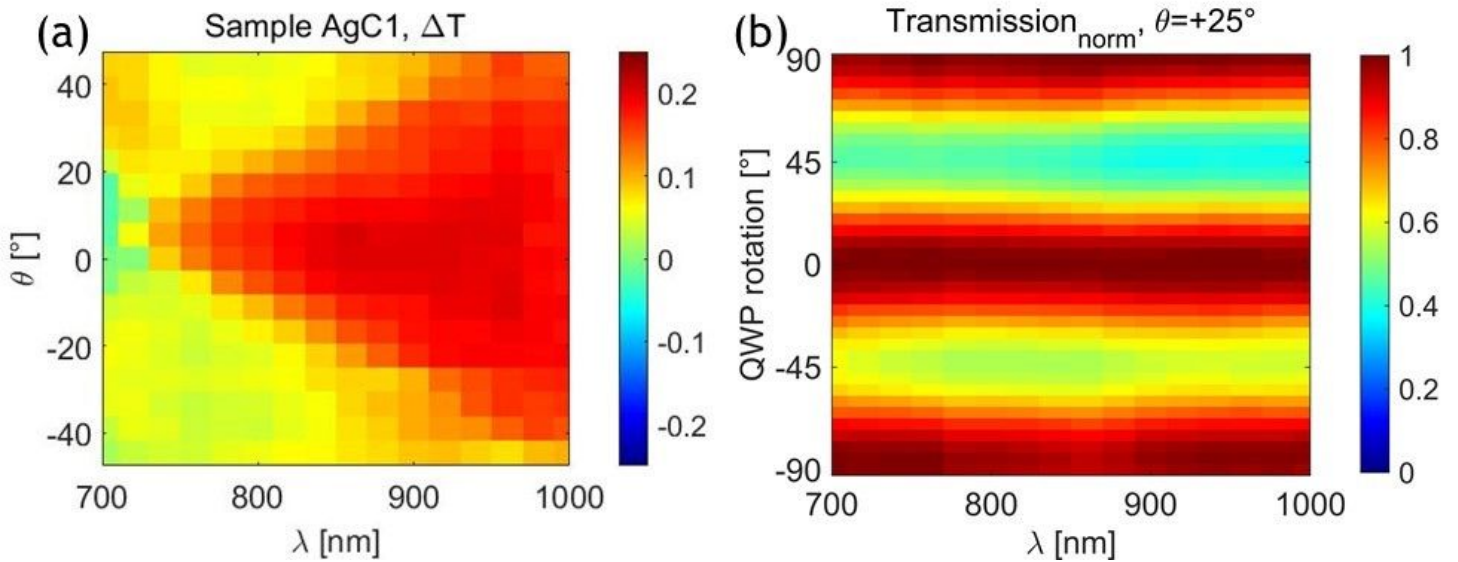
Figure 3

a Experimental λ-θ map of the ΔT difference of the light transmitted to LCP and RCP output, respectively; **b** Experimental map of the transmission spectra at varying QWP rotation at θ=25°, normalized to the sample transmission to QWP angle 0° (at θ=25°).
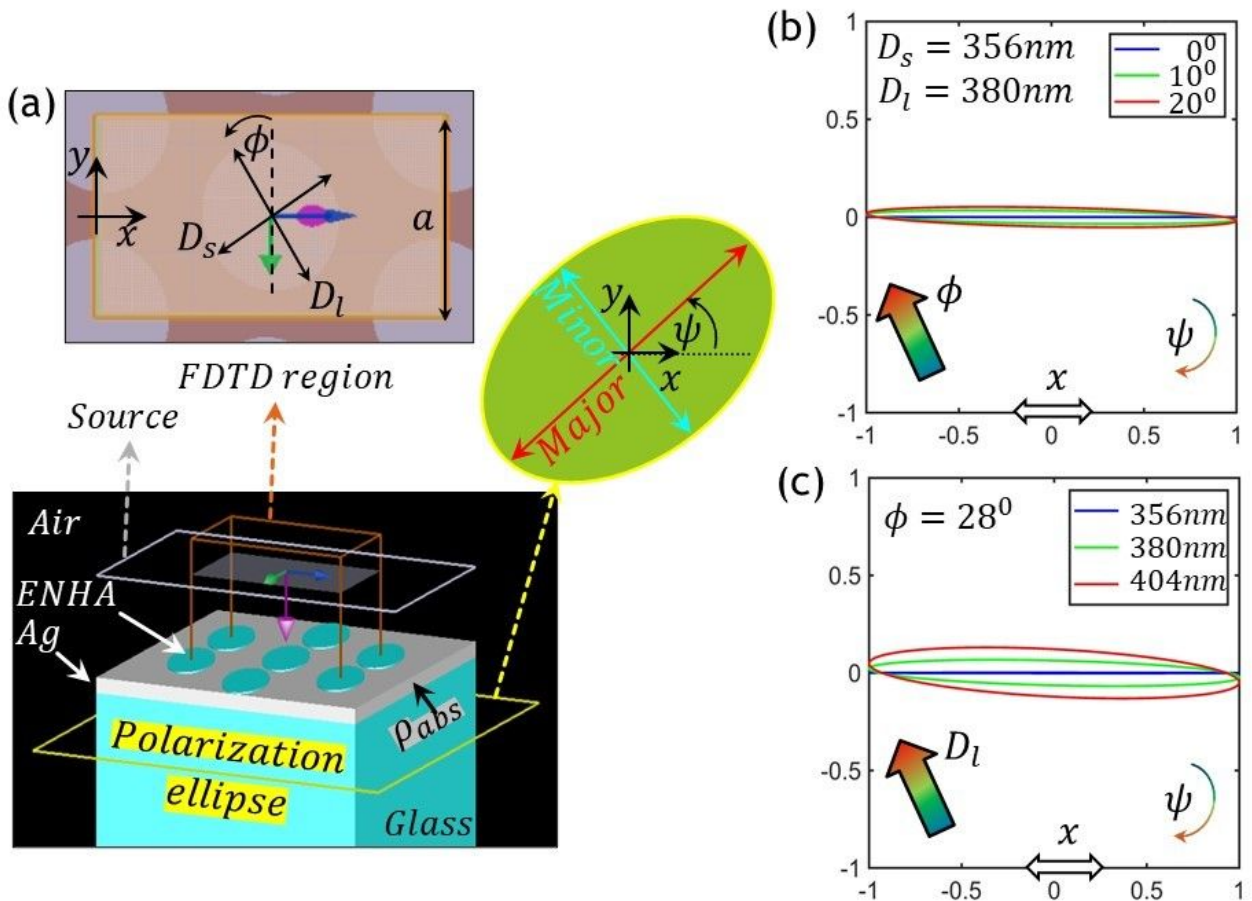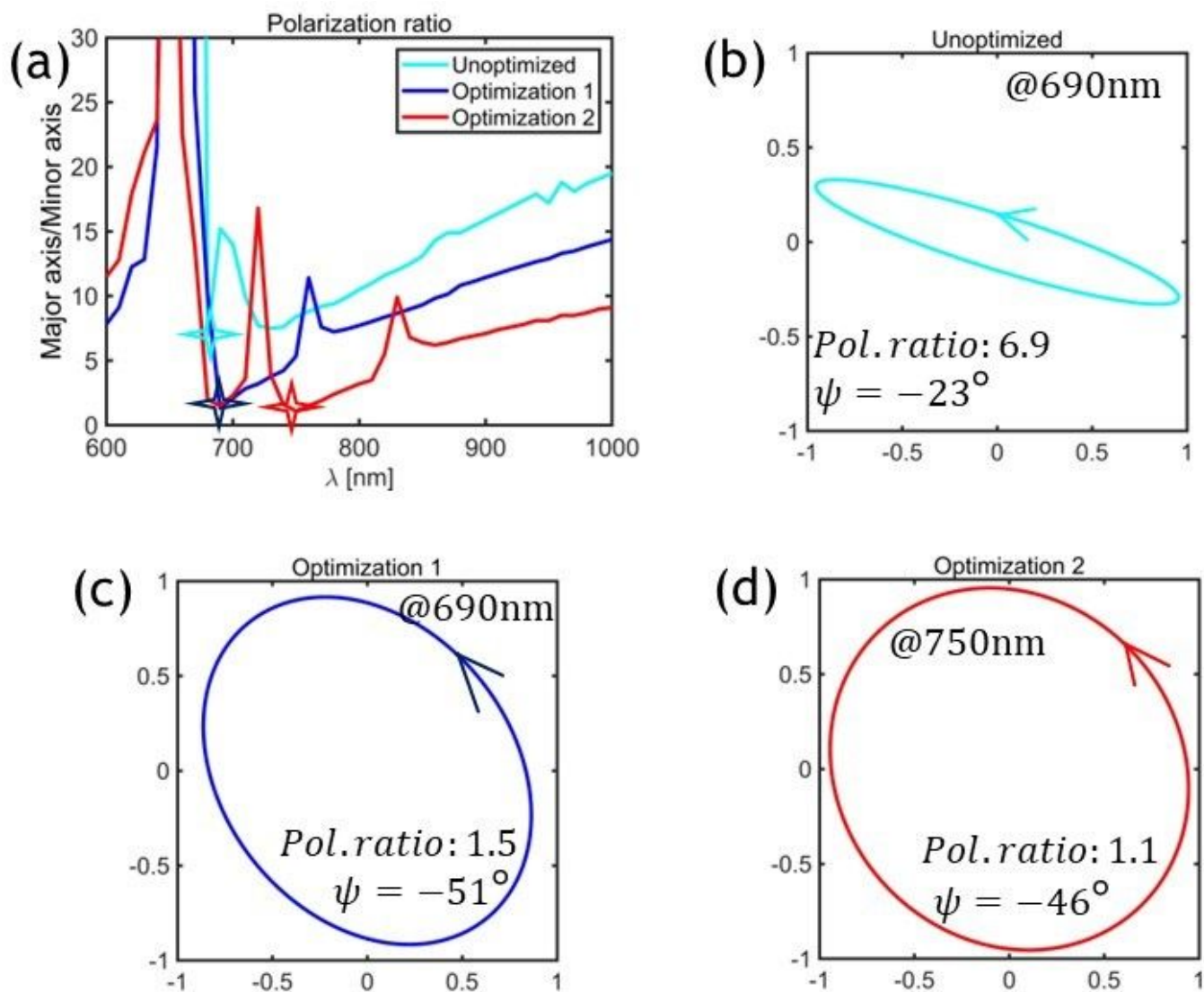

Figure 4

a Simulation set-up in xy and xz cross-sections; **b** Polarization ellipse for Dz = 356 nm, and D1 = 356 nm, as the tilt angle Φ changes; **c** Polarization ellipse for Dz = 356 nm, and Φ =28°, for different D1.

Figure 5

a Polarization ratio for three different Ag-ENHA: the unoptimized sample from this work (cyan), the Ag-ENHA sample with scaled parameters from refs. (Petronijevic et al. 2020b; Petronijevic et al. 2021b) (blue), and the new optimization of Ag-ENHA (red). **b-d** Resulting polarization ellipses at the wavelengths of the minimum polarization ratios for the ENHA **b** without optimization, **c** after Optimization 1, and **d** after Optimization 2.